CrystEngComm

ROYAL SOCIETY OF CHEMISTRY

PAPER

View Article Online
View Journal | View Issue

Cite this: *CrystEngComm*, 2020, **22**, 1645

High-performance spinel $NiMn_2O_4$ microspheres self-assembled with nanosheets by microwave-assisted synthesis for supercapacitors†

Yin Sun, Junjie Zhang, Xiannian Sun* and Naibao Huang *

Received 15th October 2019,
Accepted 3rd December 2019

DOI: 10.1039/c9ce01623f

rsc.li/crystengcomm

Spinel $NiMn_2O_4$ microspheres self-assembled with nanosheets directly grown on a 3D nickel foam were successfully prepared by a facile microwave-assisted hydrothermal process. The structural and morphology evolution behavior and the charge storage mechanism of the as-prepared samples were thoroughly characterized and assessed. It was found that the formation of the product occurred in a stepwise manner, and the steps involved were nucleation, regular growth, and a self-assembly process (from nanosheets to small microspheres and further aggregation to large microspheres), resulting in a flower-like microsphere structure. Furthermore, a study on the energy storage mechanism of the prepared spinel $NiMn_2O_4$ indicated that the diffusion-controlled process dominated charge storage at low scan rates, while the capacitive process was dominant as the scan rate increased. As a result, the as-prepared $NiMn_2O_4$ showed high specific capacitance up to 768.9 F g^{-1} at 1 A g^{-1} when measured by a charge–discharge test and excellent cycling stability (85.8% capacity retention and near 100% Coulombic efficiency after 6000 cycles at 5 A g^{-1}), which indicated that the fabricated products show a great potential in commercial supercapacitor applications.

Introduction

As a renewable green energy storage system, supercapacitors possess great prospects in mitigating energy crisis and environmental pollution due to their unique performance advantages such as high power density (>10 kW kg^{-1}), fast charge–discharge performance, long lifetime, and outstanding safety.[1–4] However, the practical application of supercapacitors is severely restricted due to their limited energy density. According to the equation of energy density (E = 1/2 CV^2), energy density (E) can be enhanced by two strategies: increasing the operating voltage window (V) or improving the specific capacitance (C).[5,6] Some strategies to widen the operating voltage window such as using organic electrolytes,[7] ionic liquids[8] or assembled asymmetrical supercapacitors[9] have been extensively studied. On the other hand, exploiting ideal electrode materials, which possess a high specific surface area, high electronic conductivity and available redox capacitance, is an effective way to improve the specific capacitance and then improve the energy density.

As a class of promising pseudocapacitive electrode materials, ternary transition metal oxides such as $NiCo_2O_4$, $MnCo_2O_4$, $CoFe_2O_4$ and $NiMn_2O_4$ having multiple oxidation states show a higher capacitance performance and superior electrochemical activities than single-component metal oxides, which enable multiple redox reactions during the energy storage process.[10–13] Among the numerous ternary transition metal oxides, $NiMn_2O_4$, as an important AB_2O_4-type spinel metal oxide, has been studied as a promising electrode material for both supercapacitors and lithium-ion batteries due to its unique advantages such as higher conductivity, more redox-active sites, relatively low cost and lower toxicity compared with those of binary metal oxides.[14,15] Recently, $NiMn_2O_4$ with different morphologies and electrochemical performances has been reported.[16–18] Wei *et al.*[19] synthesized a spinel $NiMn_2O_4$ nanosheet array with a specific capacitance of 662.5 F g^{-1} at a current density of 1 A g^{-1} *via* a facile hydrothermal method. Zhao *et al.*[20] fabricated hierarchical porous $NiMn_2O_4$ microspheres with a specific capacity of 900 mA h g^{-1} after 1000 cycles at 500 mA g^{-1}. Ray *et al.*[21] obtained porous $NiMn_2O_4$ nanoparticles *via* a sol–gel method with a specific capacitance of 875 F g^{-1} at a 2 mV s^{-1} scan rate in a redox-active hydroquinone (HQ)-incorporated aqueous electrolyte solution. Bhagwan *et al.*[22] obtained spinel $NiMn_2O_4$ nanofibers by an electrospinning process with a specific capacitance of 410 F g^{-1} at 1 A g^{-1}.

In recent years, the microwave-assisted method has been widely applied to synthesize various materials due to its own unique superiorities.[23] For example, a microwave is a non-

College of Transportation Engineering, Dalian Maritime University, Dalian 116026, China. E-mail: xsun@dlmu.edu.cn, nbhuang@dlmu.edu.cn

† Electronic supplementary information (ESI) available. See DOI: 10.1039/c9ce01623f

ionizing electromagnetic radiation with a higher penetration depth, which greatly enhances the rate of nucleation, thus reducing the synthesis time.[24] Meanwhile, the microwave treatment has an extremely low thermal gradient in the medium, which helps in forming products with uniform dimensions and high purity.[25] Furthermore, this technology also has high reaction selectivity and product yield, is energy saving, and involves accelerated kinetics, which can result in the formation of particles with uniform sizes.[14,26] It was noticed that the spinel $NiMn_2O_4$ nanosheets prepared by the hydrothermal method[19] were thin and uniform. It was reasonable to expect a lower thermal gradient and faster reaction kinetics during the hydrothermal process with the assistance of microwaves. Therefore, introducing microwaves during the hydrothermal growth process of the $NiMn_2O_4$ nanosheets may lead to their further morphology evolution, which may contribute to an improvement in the electrochemical performance.

In this paper, spinel $NiMn_2O_4$ directly grown on a 3D nickel foam was synthesized by a microwave-assisted hydrothermal process. Based on the time-dependent experiments on the growth of $NiMn_2O_4$, it was found that the $NiMn_2O_4$ nanosheets self-assembled to small microspheres and further aggregated to large microspheres due to the assistance of microwaves. The electrochemical charge storage mechanism of the obtained products was also studied by the Power law and Trasatti procedure. The tested electrochemical performances indicated that the as-prepared $NiMn_2O_4$ flower-like microspheres exhibited improved specific capacitance, which could be attributed to their self-assembled morphology evolution induced by microwaves.

Experimental

Preparation of materials

All the chemical reagents used in this work were analytical grade without any further treatment. The synthetic route is illustrated in Fig. 1. The Ni foam substance was cut into a 1 × 3 cm^2 strip and immersed into 3 M HCl for 30 min to remove the nickel oxide layer. Meanwhile, 0.316 g $KMnO_4$, 0.291 g $Ni(NO_3)_2{\cdot}6H_2O$, 0.900 g $CO(NH_2)_2$ and 0.222 g NH_4F were added to 30 mL deionized water under magnetic stirring for 1 h. A piece of the pre-treated Ni foam substrate was immersed in the mixed solution for 1 h. Then, the mixed solution and the soaked Ni foam substrate were diverted into a 100 mL Teflon-lined microwave autoclave. The microwave autoclave was loaded into a microwave hydrothermal reactor heated at 160 °C with the power set to 1000 W (XH-800G, Beijing Xianghu Science and Technology Development Co, LTD.). A microwave hydrothermal treatment time of 3 h was chosen by a time-dependent experiment. After naturally cooling to room temperature, the Ni foam was removed, followed by washing several times with deionized water and ethanol. The obtained Ni foam was dried at 70 °C for 8 h. Finally, the obtained Ni foam was annealed at 450 °C for 2 h in an Ar atmosphere.

Characterization

The crystalline structure of the synthesized $NiMn_2O_4$ sample was measured by X-ray diffraction (Rigaku, DMAX- Ultima+ diffractometer) using Co Kα radiation (λ = 1.7902 Å). The morphology and atomic content were characterized by field emission scanning electron microscopy (FE-SEM), high-resolution transmission electron microscopy (HRTEM) and energy dispersive X-ray spectroscopy (EDS). X-ray photoelectron spectroscopy (XPS) was analyzed on a Thermo ESCALAB250 XPS system (1486.6 eV, 15 kV, 10 mA, 150 W).

Electrochemical measurements

The electrochemical test was conducted on a VMP3 (EG&G) electrochemical workstation in a 6 M KOH solution using a three-electrode system, *i.e.*, the prepared $NiMn_2O_4$ electrode was used as the working electrode, a platinum net was used as the counter electrode and a saturated calomel electrode (SCE) was used as the reference electrode. The potential window of cyclic voltammetry (CV) was performed from −0.2 V to 0.5 V. The frequency of the electrochemical impedance spectroscopy (EIS) ranged from 0.01 Hz to 100 kHz. The specific capacitance of the synthesized samples was calculated by CV curves and the galvanostatic charge/discharge (GCD) curves using eqn (1) and (2), respectively.

$$C = \frac{\int_{V_1}^{V_2} i\,dV}{2mv\Delta V} \quad (1)$$

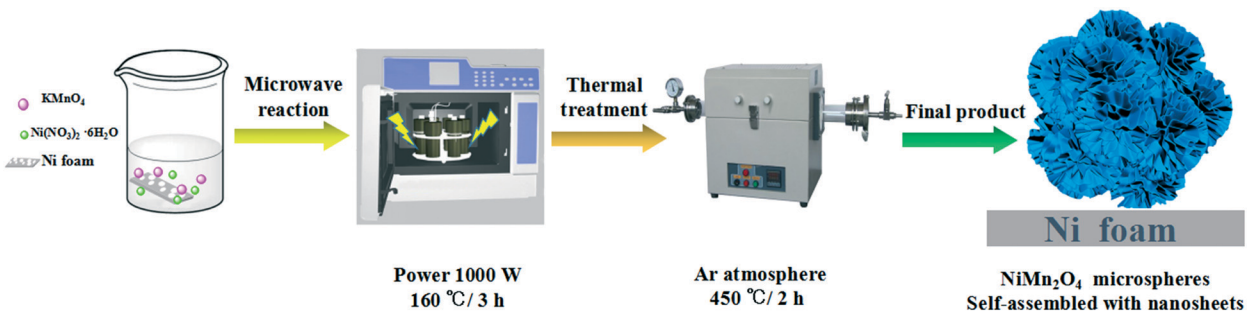

Fig. 1 Schematic image of the formation of the $NiMn_2O_4$ microspheres self-assembled with nanosheets on Ni foam.

$$C = \frac{i \cdot \Delta t}{m \cdot \Delta V} \quad (2)$$

Here, C is the specific capacitance (F g^{-1}); i is the current (A); Δt is the time of discharge (s); m is the mass (g); v is the potential scan rate (V s^{-1}) and ΔV (V_2–V_1) is the potential window (V). The measured area immersed in the electrolyte and the mass loading of the product on the Ni foam were around 1 × 1 cm^2 and 1.83 mg cm^{-2}, respectively.

Results and discussion

The obtained products were first characterized by XRD and EDS, as shown in Fig. 2. In Fig. 2(a), strong Ni diffraction peaks can be clearly identified. The relatively weaker diffraction peaks for $NiMn_2O_4$ were still evident enough to confirm that $NiMn_2O_4$ was successfully attached to the Ni foam surface. To clearly determine the crystal structure of the attached products, some products attached to the Ni foam were scratched off to be solely tested, as shown in Fig. 2(b). The relatively weak and broad diffraction peaks of the attached products implied their weak crystal characteristics, which facilitated the transport of electrolyte ions.[27,28] The measured diffraction peaks at 21.26°, 35.06°, 41.36°, 43.29°, 50.42°, 62.89°, 67.19°, and 74.08° corresponded to the (111), (220), (311), (222), (400), (422), (511), and (440) planes of the cubic phase of $NiMn_2O_4$ (JCPDS#71-0852), which has a crystallographic structure, as shown in Fig. 2(c). The X-ray energy dispersive spectrum (EDS) (Fig. 2(d)) confirms that the Ni, Mn and O elements at a molar ratio of ~1 : 2 : 4 co-exist in the final attached product, which further confirms that the obtained product is $NiMn_2O_4$.

The elemental composition and valence states of the as-prepared $NiMn_2O_4$ were investigated by XPS, as shown in Fig. 3. The elemental percentage determined by XPS is given

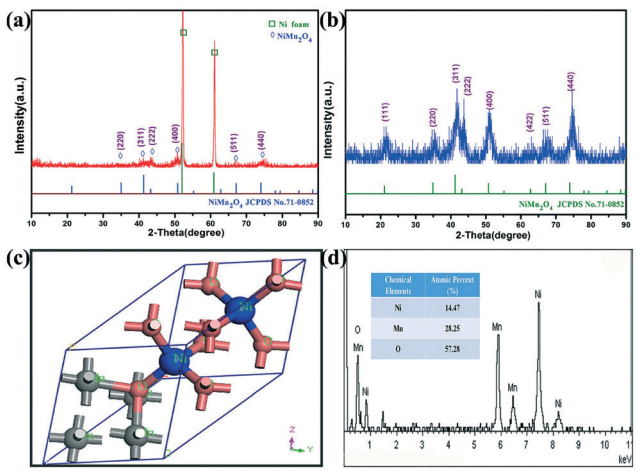

Fig. 2 (a) XRD pattern of $NiMn_2O_4$ grown on Ni foam. (b) XRD pattern of $NiMn_2O_4$ scratched from the Ni foam. (c) Crystallographic structure of $NiMn_2O_4$. (d) EDS spectrum of $NiMn_2O_4$ scratched from the Ni foam (inset shows the atomic ratio of different elements).

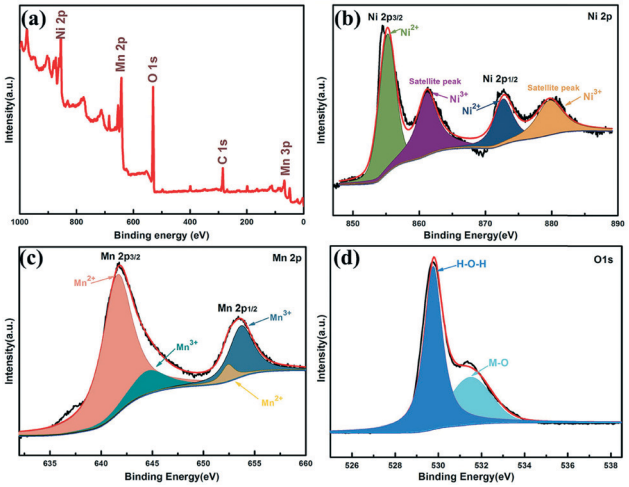

Fig. 3 XPS spectra for the as-prepared $NiMn_2O_4$: (a) a total survey, (b) Ni 2p, (c) Mn 2p, and (d) O 1s.

in Table S1.† The measured element content ratio of Ni : Mn : O in the obtained products was close to 1 : 2 : 4, which coincided with the result of the EDS test. The total survey spectrum (Fig. 3(a)) of the obtained products shows the presence of the signal peaks of Ni, Mn, O and C and there is no other impurity. The energy spectrum of Ni 2p (Fig. 3(b)) shows two spin–orbit peaks with the binding energies of 854.7 eV and 872.6 eV, corresponding to the peaks of Ni $2p_{3/2}$ and Ni $2p_{1/2}$ (the binding energy interval of the two spin–orbit peaks is 17.9 eV), together with two satellite half peaks around 861.1 and 879.3 eV, respectively. The Gaussian fitted peaks at 854.7 and 872.1 eV were assigned to the Ni^{2+} state, while the other peaks at 861.1 and 879.1 eV were assigned to the Ni^{3+} state.[13,29,30] The Mn 2p spectrum peaks in Fig. 3(c) show that the Mn 2p region consists of a spin–orbit doublet with Mn $2p_{1/2}$ and Mn $2p_{3/2}$ peaks with the binding energies of 653.4 eV and 641.7 eV, respectively. Four component peaks were fitted by the Gaussian deconvolution of the Mn 2p emission. The fitted peaks at 640.9 eV and 652.2 eV corresponded to the Mn^{2+} state, while the other two peaks at 644.3 eV and 653.5 eV were ascribed to the Mn^{3+} state.[16,31] As for the O 1s spectra (Fig. 3(d)), the fitting peaks located at 529.7 eV and 531.5 eV can be ascribed to the metal–O bond and the H–O–H bond, respectively.[16,30] Combined with previous XRD results, it can be confirmed that the prepared product is pure spinel $NiMn_2O_4$.

The morphologies and the microstructure of $NiMn_2O_4$ synthesized with the assistance of microwaves at 160 °C for 3 h were observed by both SEM and TEM; the images are displayed in Fig. 4. The optical images of the Ni foam as well as the precursor and $NiMn_2O_4$ on the Ni foam are shown in Fig. 4(a). Evidently, the microwave-assisted hydrothermal treatments and the subsequent post-calcination treatments led to the precursor formation and dehydration reaction of $NiMn_2O_4$, which presented a different colour. As shown in Fig. 4(b), massive products are evenly attached to the surface of the 3D porous Ni foam. From Fig. 4(c)–(e), it can be seen

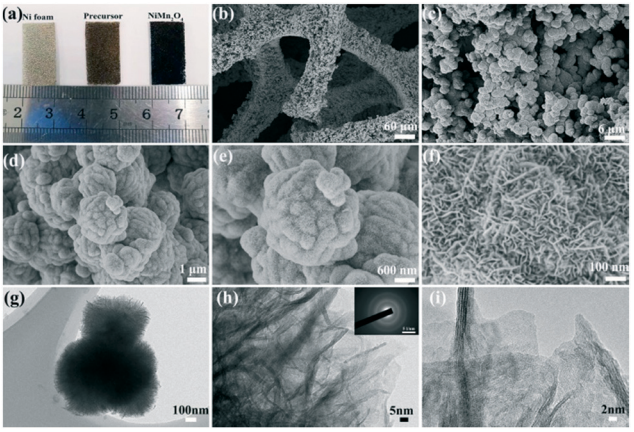

Fig. 4 (a) Optical images of the Ni foam substrate and the $NiMn_2O_4$ precursor grown on Ni foam and $NiMn_2O_4$ on Ni foam. (b–f) The low and high magnification SEM images of $NiMn_2O_4$ on Ni foam. (g–i) The low and high magnification TEM images of $NiMn_2O_4$ (inset in Fig. 4(h) shows the selected-area electron diffraction pattern).

that the as-prepared $NiMn_2O_4$ exhibits a morphology of hierarchical flower-like microspheres. Each large microsphere (~2.5 μm in diameter) consisted of many small microspheres (~0.5 μm in diameter). The further detailed image of the microsphere surface in Fig. 4(f) indicates that these microspheres consist of thin nanosheets (about 1–10 nm in thickness on average), which form many micropores (~1.3 nm, see Fig. S1†), *i.e.*, the $NiMn_2O_4$ microspheres self-assembled with nanosheets. The high specific surface area (121.2 m^2 g^{-1}, see Fig. S1†) of the as-prepared $NiMn_2O_4$ microspheres self-assembled with nanosheets could offer large contact areas between the electrode materials and the electrolyte, which was beneficial for enhancing the electrochemical properties.[32,33] The $NiMn_2O_4$ nanosheets of high density were uniformly interconnected and distributed, which can be confirmed by the TEM images shown in Fig. 4(g) and (h). The diffraction rings shown in the selected-area electron diffraction (SAED) pattern (inset of Fig. 4(h)) display dispersive distribution and no obvious lattice fringes can be observed in the high-resolution TEM (HR-TEM) image (Fig. 4(i)). Therefore, it was reasonable to assume that the as-prepared nanosheets presented weak crystallinity.[34]

In order to reveal the hierarchical microsphere formation sequence of the as-prepared $NiMn_2O_4$, a time-dependent microwave-assisted hydrothermal experiment was conducted to observe the morphology evolution during the hydrothermal process. The SEM images of the as-synthesized products at different hydrothermal times are shown in Fig. 5. According to Fig. 5(a), it took about 30 min for the autoclave to ramp up to the pre-set hydrothermal temperature. After holding for 15 min at 160 °C, thin sheet-like products consisting of nanosheets were obtained (Fig. 5(b)), which were similar to $NiMn_2O_4$ on the Ni foam prepared by the traditional hydrothermal process at the same temperature for 12 h.[19] It should be noted that many small bumps can also be observed, as shown in Fig. 5(b). After increasing the holding time from 15 min to 1 h (Fig. 5(c) and (d)), these small bumps grew steadily into small microspheres until their diameters reached ~0.5 μm. In this duration, some early-formed small microspheres attached together to form larger microspheres (~1–1.5 μm). Further holding led the small microspheres to aggregate to form large microspheres until their diameters reached ~2.5 μm (Fig. 5(e) and (f)).

Based on the observations of the above-mentioned time-dependent SEM images, a schematic illustration of the possible formation mechanism is shown in Fig. 6. In the initial reaction stage, the manganese source and the nickel source reacted with each other to nucleate on the surface of

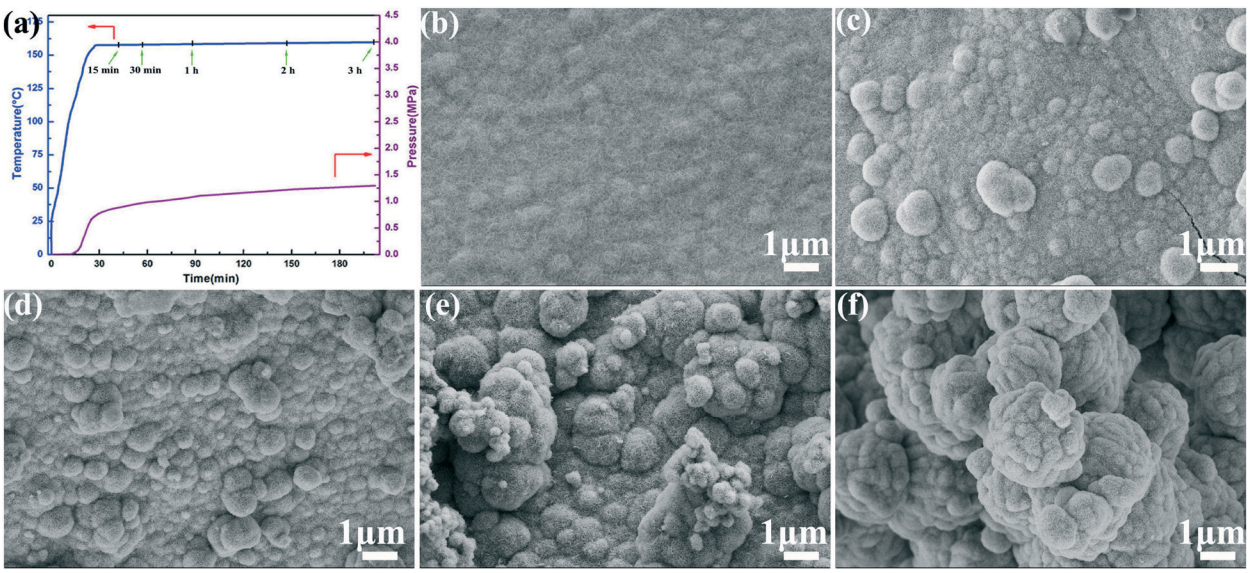

Fig. 5 (a) Temperature and pressure in the time-dependent microwave-assisted hydrothermal process. SEM images of the as-synthesized products obtained with microwave-assisted hydrothermal times of (b) 15 min, (c) 30 min, (d) 1 h, (e) 2 h and (f) 3 h.

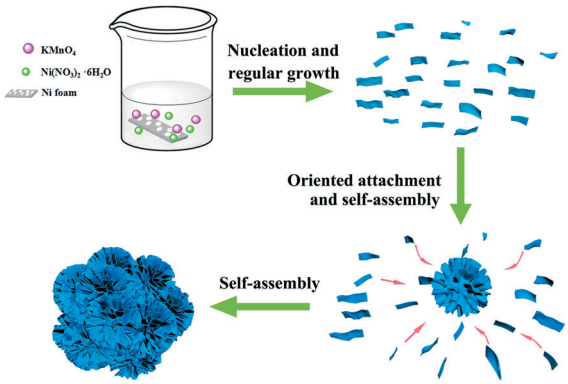

Fig. 6 Schematic illustration of the formation mechanism for the $NiMn_2O_4$ microspheres self-assembled with nanosheets.

the Ni foam and form budding nanosheets through regular growth. Due to the existence of high surface energy on the nanoscale, fresh nanosheets tend to aggregate and produce larger particles and primary ultrathin nanosheets begin to assemble together through an oriented attachment and form micro-sized fluffy spherical morphology.[35] With the further increase in the reaction time, the fluffy pellets formed in the previous stage further self-assembled into secondary microspheres driven by the lowest surface energy and the Oswald ripening mechanism.[35–37] In short, the formation of the product occurred in a stepwise manner and the steps involved were nucleation, regular growth, and the self-assembly process (from nanosheets to small microspheres and further aggregation to large microspheres), resulting in a hierarchical microsphere structure. The morphology evolution indicated that during the whole hydrothermal process, the primary nanosheets of $NiMn_2O_4$ could grow into secondary small microspheres, followed by ultimately large microspheres due to the aggregation of the small microspheres. It should be noted that the traditional hydrothermal treatment at the same temperature for 12 h could only result in the primary nanosheets of $NiMn_2O_4$. After being assisted by microwaves during the hydrothermal process, the primary nanosheets of $NiMn_2O_4$ could be produced in a much shorter time (15 min holding). More importantly, these primary nanosheets could further grow into small microspheres and self-assemble into a hierarchical microsphere microstructure, which could be attributed to the assistance of microwaves.

The electrochemical performance of the as-prepared $NiMn_2O_4$ for supercapacitor applications was evaluated by cyclic voltammetry in 6 M KOH at different scan rates, as shown in Fig. 7. From the CV curves of the $NiMn_2O_4$ electrode with a scan rate ranging from 3 mV s^{-1} to 100 mV s^{-1}, as shown in Fig. 7(a), obvious redox peaks can be observed in the CV curves at all scan rates, which indicates that the as-prepared $NiMn_2O_4$ has high pseudo-capacitance. On the other hand, all these CV curves exhibit good reversibility and the current increases on increasing the scan rate.

The CV curves shown in Fig. 7(a) can be employed to identify the charge storage mechanism of the as-prepared $NiMn_2O_4$, *i.e.*, the capacitive and diffusion-controlled electrochemical contributions to the current. The CV currents (i) and scan rates (v) can be explained by the Power law.[38,39]

$$i = av^b \tag{3}$$

It can be further rewritten as follows:

$$\log i = b \log v + \log a \tag{4}$$

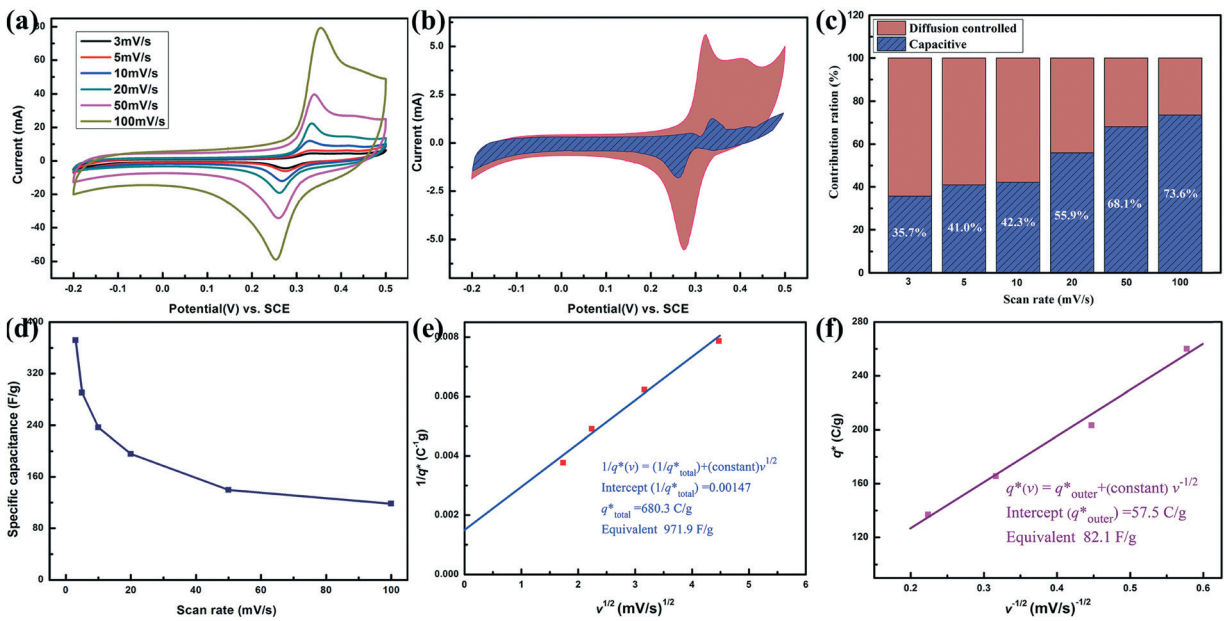

Fig. 7 (a) CV curves at different scan rates. (b) Capacity separation curves at 3 mV s^{-1}. (c) Capacity contribution ratios at different scan rates. (d) Variation in the specific capacitance with the scan rates. (e) Plot of $1/q^*$ against $v^{1/2}$. (f) Plot of q^* against $v^{-1/2}$.

Here, a is an adjustable parameter and b is the slope of the $\log i$ *vs.* $\log v$ curve. In general, the slope $b = 1$ represents that the charge/discharge processes are dominated by the capacitive response. In contrast, for an ideal diffusion-controlled electrochemical process, the slope b is 1/2. Therefore, the charge storage contribution can be calculated through the current response (i) at a given potential (V) *vs.* the scan rate (v) or the square root of the scan rate ($v^{1/2}$) using the following equation:[40–43]

$$i(V) = k_1 v + k_2 v^{1/2} \quad (5)$$

It can be further rewritten as follows:

$$i(V)/v^{1/2} = k_1 v^{1/2} + k_2 \quad (6)$$

Here, $i(V)$, $k_1 v$ and $k_2 v^{1/2}$ represent the total current response at a given potential, the capacitive contribution current and the diffusion-controlled contribution current, respectively. Moreover, k_1 and k_2 correspond to the slope and the intercept of the fitted plot between $i(V)/v^{1/}2$ and $v^{1/2}$. Thus, once the values of k_1 and k_2 are first determined by the CV curves, the current contribution by the capacitive and diffusion-controlled processes can be readily distinguished at each potential. Using the above equations, the capacity separation curves at 3 mV s^{-1} were obtained and are shown in Fig. 7(b). The blue shaded area represents the capacitive contribution, which is about 35.7% of the total capacity. In addition, the contribution ratios of charge capacity at different scan rates are summarized in Fig. 7(c). The capacitive contribution ratio increased from 35.7% to 73.6% with the scan rate increasing from 3 to 100 mV s^{-1}. Therefore, the energy storage mechanism of the prepared spinel $NiMn_2O_4$ material was dominated by the diffusion-controlled intercalation process at lower scan rates, which favoured higher capacitance.[44,45] At the same time, the dominant capacitive contribution at higher scan rates led to a fast charge/discharge process, which was conducive to a superior rate performance in the cycling processes.[46,47]

The specific capacitance at different scan rates was also calculated using eqn (1), which is shown in Fig. 7(d). It can be seen that the specific capacitance of the as-prepared $NiMn_2O_4$ electrode highly depends on the scan rate, *i.e.*, a higher scan rate leads to lower specific capacitance. At a scan rate of 100 mV s^{-1}, the calculated specific capacitance was 118.4 F g^{-1}. When the scan rate decreased to 3 mV s^{-1}, the specific capacitance increased to 371.7 F g^{-1}, which was higher than that of the reported $NiMn_2O_4$ materials prepared by other methods.[16,48,49] As a matter of fact, by slowing down the scan rate, more active sites within $NiMn_2O_4$ could be utilized by the electrolyte ions for each CV circle to contribute more charges to increase the capacitance. According to the Trasatti procedure,[50] when the scan rate $v \to 0$, full charge storage, q^*_{total}, from both the inside and outside surfaces is achieved. On the contrary, when the scan rate $v \to \infty$, only the outer surface contributes the charges, which can be employed to determine the outer surface charge storage, q^*_{outer}. By fitting the plot of $1/q^*$ against $v^{1/2}$ and q^* against $v^{-1/2}$ (ref. 38) (Fig. 7(e) and (f)), the calculated total and outer surface specific capacitances exhibited by the electrode were 971.9 F g^{-1} and 82.1 F g^{-1} at the potential window of 0.7 V, respectively. The significant difference in the specific capacitances between the total and outer surface

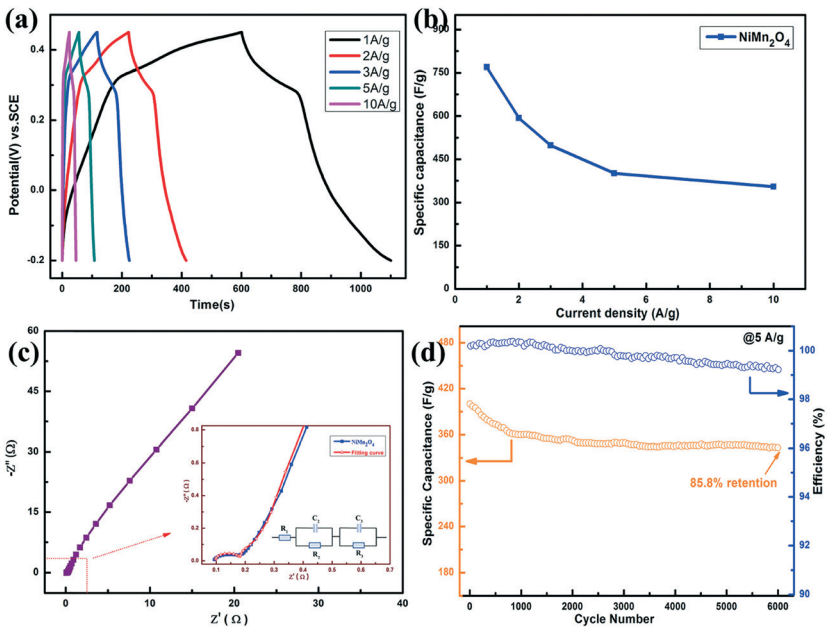

Fig. 8 (a) Charge–discharge curves at different current densities. (b) Specific capacitance measured at different current densities. (c) EIS spectra of $NiMn_2O_4$ (inset shows the fitting curve and the equivalent circuit diagram). (d) Cycling stability of the $NiMn_2O_4$ electrode at 5 A g^{-1} for 6000 cycles.

contributions indicated that the capacitance of the as-prepared spinel $NiMn_2O_4$ material was dominated by the faradaic process, which could be attributed to the more abundant and easily accessible active sites within the as-obtained products due to the hierarchical microsphere microstructure self-assembled with nanosheets. More importantly, the dense micropore structures provided easier access paths for the electrolyte.

Fig. 8(a) shows the charge–discharge curves between −0.2 and 0.45 V at different current densities from 1 to 10 A g^{-1}. Clearly, all the discharge curves have an obvious inflection point of the offset linear characteristic around 0.25 V, which is consistent with the peak potential on the CV curve. The specific capacitance of the $NiMn_2O_4$ electrode at different current densities calculated by eqn (2) is shown in Fig. 8(b). At a current density of 1 A g^{-1}, the specific capacitance of the $NiMn_2O_4$ electrode was up to 768.9 F g^{-1}, which was larger than previously reported values. The performance comparison of the $NiMn_2O_4$-based electrodes prepared by different methods is shown in Table S2, ESI.† In addition, the electrode displayed an excellent rate performance and could deliver a large specific capacitance of 354.0 F g^{-1} at a high current density of 10 A g^{-1}. The electronic resistance of the as-prepared $NiMn_2O_4$ electrode was measured by EIS. The obtained complex-plane Nyquist plots (imaginary part, $-Z''$ *vs.* real part, Z') and the values of the fitting of the EIS data are illustrated in Fig. 8(c) and Table S3,† respectively. The impedance plot in the low-frequency region was nearly linear with the inclination angle approaching 70°, which indicated the much lower diffusion resistance of the electrolyte (OH^- ions) transport to the $NiMn_2O_4$ electrode during storing energy. The enlarged view of the EIS plot at the high frequency region displays an approximate semicircle characteristic, and the charge transfer resistance (Rct) is quite small (~0.1 Ω), which indicate that the $NiMn_2O_4$ electrode possesses very low charge transfer resistance and fast diffusion/transport properties.[51–54] Additionally, the cycle performance of the $NiMn_2O_4$ electrode was measured at 5 A g^{-1} for 6000 cycles (Fig. 8(d)). The electrode exhibited good long-term cycling stability, which could be confirmed by the results that the specific capacitance remained at 85.8% and had near 100% Coulombic efficiency after 6000 cycles. Obviously, the prepared spinel $NiMn_2O_4$ microspherical material self-assembled with nanosheets exhibits an excellent electrochemical performance and is bound to have broad application prospects in high-performance supercapacitors.

Conclusions

By introducing microwave assistance in the hydrothermal process, spinel $NiMn_2O_4$ composed of unique flower-like microspheres self-assembled with nanosheets was directly grown on a 3D nickel foam. The as-obtained $NiMn_2O_4$ exhibited a specific capacitance up to 768.9 F g^{-1} at 1 A g^{-1} in the charge–discharge test and excellent cycling stability (85.8% capacity retention and near 100% Columbic efficiency after 6000 cycles at 5 A g^{-1}). The electrochemical tests revealed that the charge storage mechanism of the as-prepared $NiMn_2O_4$ was dominated by the diffusion-controlled process at low scan rates, while the capacitive process was dominant as the scan rate increased. Further calculations indicated that the as-obtained $NiMn_2O_4$ could store a maximum specific capacitance as high as ~680.3 C g^{-1} (equivalent specific capacitance ~971.9 F g^{-1}) at a potential window of 0.7 V. The exceptional electrochemical properties of the obtained product were attributed to its self-assembled hierarchical microsphere microstructure assisted by microwaves during the hydrothermal process; thus, it shows a great potential in commercial supercapacitor applications.

Conflicts of interest

There are no conflicts to declare.

Acknowledgements

This work was financially supported by the National Key Research and Development Program of China (2016YFB0101206), the National Natural Science Foundation of China (21676040, 51879018, 21276036), the Dalian Science and Technology Innovation Funds (2018J12GX053) and the Fundamental Research Funds for the Central Universities (3132019328, 3132019327).

References

1 Y. Wang, Y. Song and Y. Xia, *Chem. Soc. Rev.*, 2016, **45**, 5925–5950.
2 G. P. Wang, L. Zhang and J. J. Zhang, *Chem. Soc. Rev.*, 2012, **41**, 797–828.
3 J. Yan, Q. Wang, T. Wei and Z. Fan, *Adv. Energy Mater.*, 2014, **4**, DOI: 10.1002/aenm.201300816.
4 H. Jiang, P. S. Lee and C. Z. Li, *Energy Environ. Sci.*, 2013, **6**, 41–53.
5 J. T. Zhang, J. W. Jiang, H. L. Li and X. S. Zhao, *Energy Environ. Sci.*, 2011, **4**, 4009–4015.
6 J. L. Liu, J. Wang, C. H. Xu, H. Jiang, C. Z. Li, L. L. Zhang, J. Y. Lin and Z. X. Shen, *Adv. Sci.*, 2018, **5**, DOI: 10.1002/advs.201700322.
7 H. J. Yu, J. H. Wu, L. Q. Fan, S. C. Hao, J. M. Lin and M. L. Huang, *J. Power Sources*, 2014, **248**, 1123–1126.
8 T. Y. Kim, H. W. Lee, M. Stoller, D. R. Dreyer, C. W. Bielawski, R. S. Ruoff and K. S. Suh, *ACS Nano*, 2011, **5**, 436–442.
9 H. Wang, Z. Xu, A. Kohandehghan, Z. Li, K. Cui, X. Tan, T. J. Stephenson, C. K. King'ondu, C. M. B. Holt, B. C. Olsen, J. K. Tak, D. Harfield, A. O. Anyia and D. Mitlin, *ACS Nano*, 2013, **7**, 5131–5141.
10 A. K. Mondal, D. Su, S. Chen, X. Xie and G. Wang, *ACS Appl. Mater. Interfaces*, 2014, **6**, 14827–14835.
11 A. K. Mondal, D. Su, S. Chen, A. Ung, H.-S. Kim and G. Wang, *Chem. – Eur. J.*, 2015, **21**, 1526–1532.
12 S. G. Mohamed, C.-J. Chen, C. K. Chen, S.-F. Hu and R.-S. Liu, *ACS Appl. Mater. Interfaces*, 2014, **6**, 22701–22708.

13 W. Kang, Y. Tang, W. Li, X. Yang, H. Xue, Q. Yang and C.-S. Lee, *Nanoscale*, 2015, **7**, 225–231.
14 S. K. Meher, P. Justin and G. R. Rao, *ACS Appl. Mater. Interfaces*, 2011, **3**, 2063–2073.
15 H. Kim, D.-H. Seo, H. Kim, I. Park, J. Hong, K.-Y. Park and K. Kang, *Chem. Mater.*, 2012, **24**, 720–725.
16 M. Zhang, S. Guo, L. Zheng, G. Zhang, Z. Hao, L. Kang and Z.-H. Liu, *Electrochim. Acta*, 2013, **87**, 546–553.
17 J. Huang, W. Wang, X. Lin, C. Gu and J. Liu, *J. Power Sources*, 2018, **378**, 677–684.
18 S. Peng, L. Li, Y. Hu, M. Srinivasan, F. Cheng, J. Chen and S. Ramakrishna, *ACS Nano*, 2015, **9**, 1945–1954.
19 H. M. Wei, J. X. Wang, L. Yu, Y. Y. Zhang, D. W. Hou and T. F. Li, *Ceram. Int.*, 2016, **42**, 14963–14969.
20 S. Zhao, H. Li, Z. Jian, Y. Xing and S. Zhang, *RSC Adv.*, 2018, **8**, 41749–41755.
21 A. Ray, A. Roy, M. Ghosh, J. Alberto Ramos-Ramón, S. Saha, U. Pal, S. K. Bhattacharya and S. Das, *Appl. Surf. Sci.*, 2019, **463**, 513–525.
22 J. Bhagwan, S. Rani, V. Sivasankaran, K. L. Yadav and Y. Sharma, *Appl. Surf. Sci.*, 2017, **426**, 913–923.
23 Y.-J. Zhu and F. Chen, *Chem. Rev.*, 2014, **114**, 6462–6555.
24 C. Yuan, X. Zhang, L. Su, B. Gao and L. Shen, *J. Mater. Chem.*, 2009, **19**, 5772.
25 V. Polshettiwar, B. Baruwati and R. S. Varma, *ACS Nano*, 2009, **3**, 728–736.
26 L. Peng, X. Ji, H. Wan, Y. Ruan, K. Xu, C. Chen, L. Miao and J. Jiang, *Electrochim. Acta*, 2015, **182**, 361–367.
27 Y. Sun, N. Huang, X. Sun, D. Wang, J. Zhang, S. Qiao and Z. Gao, *Int. J. Hydrogen Energy*, 2017, **42**, 20016–20025.
28 H. Y. Lee and J. B. Goodenough, *J. Solid State Chem.*, 1999, **144**, 220–223.
29 Z. Wang, Z. Zhu, C. Zhang, C. Xu and C. Chen, *Electrochim. Acta*, 2017, **230**, 438–444.
30 H. H. Nan, W. Q. Ma, Z. X. Gu, B. Y. Geng and X. J. Zhang, *RSC Adv.*, 2015, **5**, 24607–24614.
31 J. Pu, J. Wang, X. Q. Jin, F. L. Cui, E. H. Sheng and Z. H. Wang, *Electrochim. Acta*, 2013, **106**, 226–234.
32 H. S. Jiang, W. J. Sun, W. Y. Li, Z. Wang, X. Y. Zhou, Z. X. Wu and J. B. Bai, *Front. Chem.*, 2019, **7**, DOI: 10.3389/fchem.2019.00595.
33 W. Y. Li, B. J. Zhang, R. J. Lin, S. Ho-Kimura, G. J. He, X. Y. Zhou, J. Q. Hu and I. P. Parkin, *Adv. Funct. Mater.*, 2018, **28**, DOI: 10.1002/adfm.201705937.
34 L. Wu, Y. Hu, X. P. Zhang, J. Q. Liu, X. Zhu and S. K. Zhong, *J. Power Sources*, 2018, **374**, 40–47.
35 T. Li, G. H. Li, L. H. Li, L. Liu, Y. Xu, H. Y. Ding and T. Zhang, *ACS Appl. Mater. Interfaces*, 2016, **8**, 2562–2572.
36 C. Yuan, X. Zhang, L. Su, B. Gao and L. Shen, *J. Mater. Chem.*, 2009, **19**, 5772–5777.
37 P. P. Lv, H. L. Zhao, Z. P. Zeng, C. H. Gao, X. Liu and T. H. Zhang, *Appl. Surf. Sci.*, 2015, **329**, 301–305.
38 M. Sathiya, A. S. Prakash, K. Ramesha, J. M. Tarascon and A. K. Shukla, *J. Am. Chem. Soc.*, 2011, **133**, 16291–16299.
39 J. Wang, J. Polleux, J. Lim and B. Dunn, *J. Phys. Chem. C*, 2007, **111**, 14925–14931.
40 K. Zhang, M. H. Park, L. M. Zhou, G. H. Lee, W. J. Li, Y. M. Kang and J. Chen, *Adv. Funct. Mater.*, 2016, **26**, 6728–6735.
41 D. L. Chao, C. R. Zhu, P. H. Yang, X. H. Xia, J. L. Liu, J. Wang, X. F. Fan, S. V. Savilov, J. Y. Lin, H. J. Fan and Z. X. Shen, *Nat. Commun.*, 2016, **7**, DOI: 10.1038/ncomms12122.
42 D. L. Chao, P. Liang, Z. Chen, L. Y. Bai, H. Shen, X. X. Liu, X. H. Xia, Y. L. Zhao, S. V. Savilov, J. Y. Lin and Z. X. Shen, *ACS Nano*, 2016, **10**, 10211–10219.
43 X. Wang, L. Ma and J. Sun, *ACS Appl. Mater. Interfaces*, 2019, **11**, 41297–41303.
44 F. Wan, L. Zhang, X. Dai, X. Wang, Z. Niu and J. Chen, *Nat. Commun.*, 2018, **9**, 1656.
45 X. Wang, L. Ma, P. Zhang, H. Wang, S. Li, S. Ji, Z. Wen and J. Sun, *Appl. Surf. Sci.*, 2019, 144207, DOI: 10.1016/j.apsusc.2019.144207.
46 C. T. Zhao, C. Yu, M. D. Zhang, H. W. Huang, S. F. Li, X. T. Han, Z. B. Liu, J. Yang, W. Xiao, J. N. Liang, X. L. Sun and J. S. Qiu, *Adv. Energy Mater.*, 2017, **7**, DOI: 10.1002/aenm.201602880.
47 M. M. Yin, X. T. Feng, D. Zhao, Y. Zhao, H. S. Li, W. Zhou, H. B. Liu, X. P. Bai, H. X. Wang, C. H. Feng and Q. Z. Jiao, *ACS Sustainable Chem. Eng.*, 2019, **7**, 6122–6130.
48 U. J. Chavan and A. A. Yadav, *J. Mater. Sci.: Mater. Electron.*, 2016, **28**, 4958–4964.
49 C. H. Wu, J. S. Ma and C. H. Lu, *Curr. Appl. Phys.*, 2012, **12**, 1190–1194.
50 S. Ardizzone, G. Fregonara and S. Trasatti, *Electrochim. Acta*, 1990, **35**, 263–267.
51 G. J. He, M. Qiao, W. Y. Li, Y. Lu, T. T. Zhao, R. J. Zou, B. Li, J. A. Darr, J. Q. Hu, M. M. Titirici and I. P. Parkin, *Adv. Sci.*, 2017, **4**, DOI: 10.1002/advs.201600214.
52 S. K. Meher, P. Justin and G. R. Rao, *Electrochim. Acta*, 2010, **55**, 8388–8396.
53 X. Zhang, W. Shi, J. Zhu, W. Zhao, J. Ma, S. Mhaisalkar, T. L. Maria, Y. Yang, H. Zhang, H. H. Hng and Q. Yan, *Nano Res.*, 2010, **3**, 643–652.
54 G. He, M. Ling, X. Han, D. I. Abou El Amaiem, Y. Shao, Y. Li, W. Li, S. Ji, B. Li, Y. Lu, R. Zou, F. Ryan Wang, D. J. L. Brett, Z. Xiao Guo, C. Blackman and I. P. Parkin, *Energy Storage Mater.*, 2017, **9**, 119–125.

